

1 **Intensive photochemical oxidation in the marine atmosphere:**
2 **Evidence from direct radical measurements**

3 Guoxian Zhang^{1,2}, Renzhi Hu^{1, *}, Pinhua Xie^{1,2,3, **}, Changjin Hu¹, Xiaoyan Liu⁴,
4 Liujun Zhong¹, Haotian Cai¹, Bo Zhu⁵, Shiyong Xia⁵, Xiaofeng Huang⁵, Xin Li⁶,
5 Wenqing Liu¹

6 ¹ Key Laboratory of Environment Optics and Technology, Anhui Institute of Optics and Fine
7 Mechanics, HFIPS, Chinese Academy of Sciences, Hefei, China

8 ² University of Science and Technology of China, Hefei, China

9 ³ College of Resources and Environment, University of Chinese Academy of Science, Beijing,
10 China

11 ⁴ School of Pharmacy, Anhui Medical University, Hefei, China

12 ⁵ Key Laboratory for Urban Habitat Environmental Science and Technology, School of
13 Environment and Energy, Peking University Shenzhen Graduate School, Shenzhen, China

14 ⁶ State Key Joint Laboratory of Environmental Simulation and Pollution Control, College of
15 Environmental Sciences and Engineering, Peking University, Beijing, China

16

17 ***Correspondence to:** Renzhi Hu, Key Laboratory of Environment Optics and
18 Technology, Anhui Institute of Optics and Fine Mechanics, HFIPS, Chinese Academy
19 of Sciences, Hefei, China

20 ****Correspondence to:** Pinhua Xie, University of Science and Technology of China,
21 Hefei, China

22 **Email addresses:** rzhu@aiofm.ac.cn (Renzhi Hu); phxie@aiofm.ac.cn (Pinhua Xie)

23

24 **Abstract:** Comprehensive observations of hydroxyl (OH) and hydroperoxy (HO₂)
25 radicals were conducted in October 2019 at a coastal continental site in the Pearl
26 River Delta (YMK site, 22.55°N, 114.60°E). The daily maximum OH and HO₂
27 concentrations were $(4.7\text{--}9.5) \times 10^6 \text{ cm}^{-3}$ and $(4.2\text{--}8.1) \times 10^8 \text{ cm}^{-3}$, respectively. The
28 synchronized air mass transport from the northern cities and the South China Sea
29 exerted a time-varying influence on atmospheric oxidation. Under a typical ocean-
30 atmosphere (OCM), reasonable measurement model agreement was achieved for both
31 OH and HO₂ using a 0-D chemical box model incorporating the regional atmospheric
32 chemistry mechanism version 2-Leuven isoprene mechanism (RACM2-LIM1), with
33 daily averages of $4.5 \times 10^6 \text{ cm}^{-3}$ and $4.9 \times 10^8 \text{ cm}^{-3}$, respectively. Land mass (LAM)
34 influence promoted more active photochemical processes, with daily averages of 7.1
35 $\times 10^6 \text{ cm}^{-3}$ and $5.2 \times 10^8 \text{ cm}^{-3}$ for OH and HO₂, respectively. Heterogeneous uptake
36 had certain effects on HO_x chemistry, but the influence of the halogen mechanism
37 was limited by NO_x level. Intensive photochemistry occurred after precursor
38 accumulation, allowing local net ozone production comparable with surrounding
39 suburban environments (5.52 ppb/h during the LAM period). Rapid oxidation process
40 was accompanied by a higher diurnal nitrous acid (HONO) concentration (> 400 ppt).
41 After a sensitivity test, HONO-related chemistry elevated the ozone production rate
42 by 33% and 39% during the LAM and OCM periods, respectively. The nitric acid
43 (P(HNO₃)) and sulfuric acid (P(H₂SO₄)) formation rates also increased
44 simultaneously (~43% and ~48% for LAM and OCM sectors, respectively). Without
45 the HONO constraint, simulated O₃ decreased from ~75 ppb to a global background
46 (~35 ppb), and daytime HONO concentrations were reduced to a low level (~70 ppt).
47 For coastal cities, the particularity of the HONO chemistry tends to influence the
48 ozone-sensitive system and eventually magnifies the background ozone. Therefore,
49 the promotion of oxidation by elevated precursors deserves a lot of attention when
50 aiding pollution mitigation policies.

51 **Keywords:** FAGE-LIF; OH and HO₂ radicals; Atmospheric oxidation; Marine
52 boundary layer; Precursors;

1 Introduction

The marine boundary layer (MBL) occupies 71% of the planetary boundary layer, is a massive active carbon sink on Earth, and plays an irreplaceable role in coping with global climate change (Stone et al., 2012; Woodward-Massey et al., 2022a; Liu et al., 2022a). As a typical background atmosphere on the Earth, the MBL is equivalent to a natural smog chamber with limited anthropogenic emissions and is characterized by low NO_x (the sum of nitric oxide (NO) and nitrogen dioxide (NO₂)) and non-methane hydrocarbons (NMHCs) under a layer of clean air (Woodward-Massey et al., 2022a). The lifetime of OH radical, a key oxidant, is on the order of a few hundred milliseconds (Fuchs et al., 2012). Due to the scarcity of oxidation precursors, including nitrous acid (HONO), formaldehyde (HCHO), and NMHCs, the reaction between O¹D and water vapor generally dominates the radical initiation pathway in the marine environment. For example, in a tropical boundary layer observation experiment (reactive halogens in the marine boundary layer, RHaMBLe), ozone photolysis was found to account for 70% of the OH radical source based on the master chemical mechanism (MCM) (Whalley et al., 2010). The vital role of ozone photolysis is contrasting with typical polluted and semi-polluted areas investigated in a series of field campaigns, in which the propagation routes were found to dominate the radical source (Yang et al., 2021a; Tan et al., 2019a). Therefore, studying the radical chemistry in the MBL provides a valuable opportunity to test the current understanding of atmospheric oxidation mechanisms in a natural setting.

Since the earliest observations off the coast of northern Norfolk in the Weybourne Atmospheric Observatory Summer Experiment in June 1995 (WAOSE95), more observations and simulations of radical chemistry in the MBL environment have been conducted using ground-based, airborne, and shipborne instruments (Qi et al., 2007; Kanaya et al., 2002; Kanaya et al., 2001; Mallik et al., 2018; Woodward-Massey et al., 2022b; Carpenter et al., 2011; Grenfell et al., 1999; Brauers et al., 2001; Whalley et al., 2010). Most field measurements have yielded well-reproduced OH and HO₂ concentration profiles via chemical mechanisms, with differences of within ~20%.

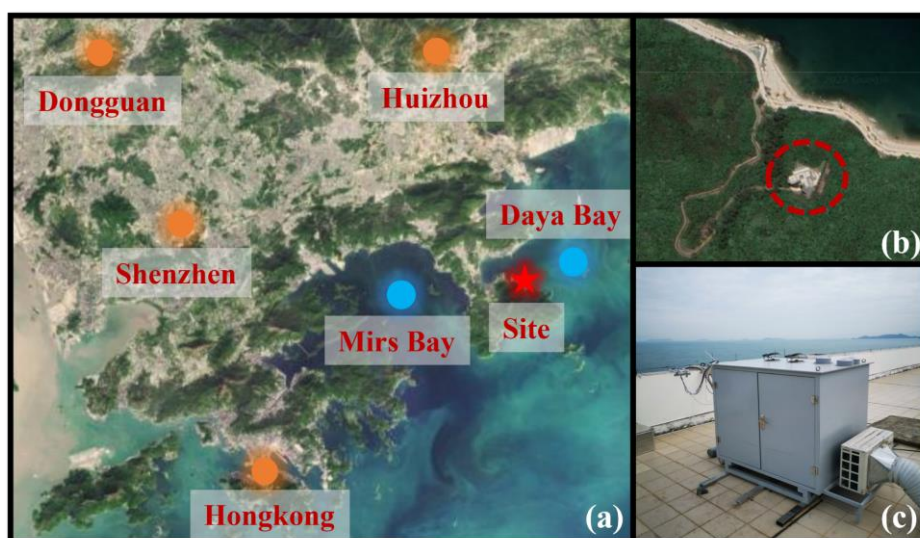
82 However, the base model is not sufficient to describe the radical chemistry in some
83 exceptional cases, especially in regard to the HO₂ radical. Considering the practical
84 association between halogen (Cl, Br, and I) chemistry and heterogeneous chemistry in
85 marine new particle formation, particularly the involvement of heterogeneous iodine-
86 organic chemistry, exploring the synchronous influence of these mechanisms on HO_x
87 (OH and HO₂) radical chemistry in the MBL region is a worthy endeavor (Xu et al.,
88 2022; Huang et al., 2022). The mixing of air masses of continental and marine origins
89 can lead to more variability in radical concentrations. During seasonal measurements
90 of both OH and HO₂ in the Atlantic Ocean, variance analysis indicated that around 70%
91 of the variance of OH and HO₂ was due to diurnal behavior (in the form of photolysis
92 frequency), while the remaining variance was attributed to long-term seasonal cycles
93 (in the form of the changes in O₃, CO and air mass contribution) (Vaughan et al.,
94 2012).

95 The Chinese economy has undergone rapid development in recent years, and the
96 co-occurrence of primary and secondary regional pollution has become a severe
97 problem (Lu et al., 2019; Liu et al., 2022c). The interactions between air pollutants
98 from upwind cities, shipping vessels, and other anthropogenic emissions lead to
99 precursor accumulation (Sun et al., 2020; Zeren et al., 2022). The background ozone
100 concentration in key regions of China has increased year by year, highlighting the
101 significant influence of anthropogenic activities on the atmospheric oxidation in
102 background regions in China (Wang et al., 2009; Chen et al., 2022). However, little
103 research has been dedicated to the radical chemistry and oxidation mechanism in
104 regions with both coastal and continental features. To fill this research gap, in this
105 study, a field campaign was conducted on photochemistry in the MBL at a coastal site
106 in the Pearl River Delta. The OH and HO₂ radicals associated with other related
107 species were measured in October 2019, and the radical-related oxidation process was
108 identified to determine the photochemical efficiency in the marine atmosphere.

109 **2 Materials and methods**

110 2.1 Site description

111 As shown in Fig. 1(a), this observation campaign lasted for 11 days from
112 October 18 to October 28, 2019, in Yangmeikeng (YMK, 22.55°N, 114.60°E), a
113 coastal site in Shenzhen, Pearl River Delta. As the core city of the Greater Bay Area,
114 Shenzhen is bordered by Dongguan to the north, Huizhou to the east, and Hong Kong
115 to the south. The YMK site is on the Dapeng Peninsula, to the southeast of Shenzhen,
116 between Mirs Bay and Daya Bay. As it is adjacent to the port of Hong Kong,
117 precursors from ship emissions may influence the atmospheric chemistry. The site is a
118 part of Shenzhen Ecological Monitoring Center station, approximately 35 m above
119 sea level, and the sea is approximately 150 m to the east. No apparent local emissions
120 exist, and the surrounding forest is lush (Fig. 1(b)). Previous literatures reported the
121 monoterpene concentration in the YMK site, with a daily mean of 0.187 ppb (Zhu et
122 al., 2021). Abundant biogenic emissions will likely influence the local chemistry. In
123 addition to anthropogenic and vegetation emissions, the site is also affected by the
124 synchronization of plumes from northern cities and the South China Sea (Niu et al.,
125 2022; Xia et al., 2021). Due to its significant time-varying pollution characteristics,
126 this area is an ideal site for studying the effects of plume transport on atmospheric
127 oxidation.



128

129 **Fig. 1.** Details of the observation site.(a) The location of the measurement site and surrounding cities. The satellite
130 map data is extracted from Google Earth.(b) Th close shot of the measurement site location.(c) The actual image
131 for the LIF-Box.

132 Using the hybrid single-particle Lagrangian integrated trajectory (HYSPLIT)

133 model, the 24-h backward trajectories on special days were obtained. In Fig. S1, the
134 red, blue, and green trajectories represent the results at altitudes of 100, 500, and 1000
135 m above ground level, respectively. Two typical transportation pathways dominated
136 the air parcels. One originated from the northern megacities in the Pearl River Delta
137 (defined as the land mass, LAM), especially on October 18, 19, and 27. In contrast, a
138 clean air mass from the east or northeast was mainly transported to the observation
139 site from the ocean (defined as the ocean mass, OCM), with representative episodes
140 on October 22, 25, and 26.

141 **2.2 Instrumentation**

142 **2.2.1 HO_x radical measurements**

143 The OH and HO₂ radicals were measured via laser-induced fluorescence (LIF).
144 The OH radical can be directly measured by exciting the fluorescence using a 308-nm
145 laser. HO₂ is converted into the OH radical via chemical transformation and then
146 detected in the form of OH radical. The self-developed instrument, the Anhui Institute
147 of Optics Fine Mechanics-LIF (AIOFM-LIF), was used to conduct the measurements
148 (Zhang et al., 2022a; Wang et al., 2021; Wang et al., 2019). This system has been used
149 in key regions of China, including the Yangtze River Delta, Pearl River Delta, and
150 Chengdu-Chongqing region, and achieved good performance in a comparison
151 experiment with a LIF system jointly developed by Forschungszentrum Jülich and
152 Peking University (PKU-LIF) (Zhang et al., 2022b).

153 The system and detection interference process have been described in detail in
154 previous studies (Zhang et al., 2022a). Briefly, the system consists of a laser output
155 module, a radical detection module, and a control and data acquisition module. These
156 modules are integrated into a sampling box with constant temperature and humidity
157 control (Fig. 1(c)). The laser output module is a union of an Nd:yttrium-aluminum-
158 garnet (YAG) solid-state laser, a 532-nm laser output, and a tunable dye laser. The
159 radical detection module utilized a single pass laser configuration, and the laser beam
160 was amplified to a diameter of 8 mm. OH and HO₂ fluorescence cells are combined in
161 parallel and share a common axial optical path. The 308-nm laser is introduced into

162 the HO₂ cell first and then into the OH cell via an 8-m fiber. To maintain the detection
163 efficiency, the power in the OH fluorescence cell should be at least 15 mW. In the
164 detection process, a set of lenses was deployed and positioned in front of the
165 microchannel plate detector (MCP) to boost the fluorescence collection capacity. Each
166 MCP detector contains a timing control instrument to optimize the signal-to-noise
167 ratio (SNR) of the fluorescence detection. Efficient ambient air sampling was
168 achieved using an aluminum nozzle (0.4 mm orifice), and the pressure in the chamber
169 was maintained at 400 Pa via a vortex vacuum pump (XDS35i, Edwards) to reduce
170 fluorescence quenching.

171 A wavelength modulation for the background measurement that periodically
172 switches from an on-resonant state to a non-resonant state has been widely used to
173 obtain spectral zero. Due to the synchronous reaction at 308nm, wavelength
174 modulation is not applicable to ozone photolysis interference. Through laboratory
175 experiments, at 20 mW laser energy, every 1% water vapor concentration and 50 ppb
176 ozone concentration can generate a $2.5 \times 10^5 \text{ cm}^{-3}$ OH concentration. The results in
177 this paper have subtracted the ozone photolysis interference (Fig. S2). In terms of
178 system design, the AIOFM-LIF system incorporates a short-length inlet design to
179 minimize interferences from ozonolysis and other unknown factors (the distance from
180 radical sampling to fluorescence excitation is ~150 mm). An OH measurement
181 comparison with an interference-free instrument, PKU-LIF, was conducted in a real
182 atmosphere in a previous study (Zhang et al., 2022b). The ozonolysis interference on
183 the measurement consistency of both systems was excluded under high-VOCs
184 condition. Overall, the key parameters related to ozonolysis reactions (O₃, alkenes,
185 isoprene and NO_x) in YMK was similar to that during the intercomparison
186 experiment, implies that the chemical conditions do not favor the generation of
187 potential interference to OH measurement (Table S1). For HO₂ measurement, the NO
188 gas was mixed with 2% in N₂ to achieve HO₂-to-OH conversion. NO was passed
189 through a ferrous sulfate filter to remove impurities (NO₂, HONO, and so on) before
190 being injected into the detection cell. The NO concentration ($\sim 1.6 \times 10^{12} \text{ cm}^{-3}$)

191 corresponding to a conversion efficiency of ~15% was selected to avoid RO₂→HO₂
192 interference (especially from RO₂ radicals derived from long-chain alkanes (C ≥ 3),
193 alkenes, and aromatic hydrocarbons). Previous study denoted that the percentage
194 interference from alkene-derived RO₂ under these operating conditions was no more
195 than 5% (Wang et al., 2021).

196 A standard HO_x radical source was used to complete the calibration of the
197 detection sensitivity (Wang et al., 2020). The radical source is based on the
198 simultaneous photolysis of H₂O/O₂ by a 185 nm mercury lamp. Humidified air flow is
199 introduced to produce equal amounts of OH and HO₂ radicals after passing the
200 photolysis region. The flow remained in a laminar condition with a maximum flow
201 rate of 20 SLM (standard liters per minute). As the luminous flux in photolysis region
202 is difficult to accurately measure, the linearly correlation between ozone concentration
203 and 185 nm light flux was established. Ozone concentration in the flow tube was
204 measured by a home-made Cavity Ring Down Spectrometer (CRDS, and the
205 detection limit is 15 ppt@30 s, 1σ). Mercury lamp intensity is adjusted to establish.
206 The instrument was calibrated every 1 or 2 days (except for shutdown during rainy
207 periods), and the sensitivity used for the data processing was an average of all of the
208 calibration results. In the YMK campaign, the humidity varied between 40 – 80% (Fig.
209 S3). In order to test different atmospheric conditions, both low (~40%) and high
210 (~70%) levels of water vapor were selected to produce OH and HO₂ radicals for
211 calibration, and the corresponding HO_x concentration obtained from the standard
212 source was $1.0 \times 10^9 \text{ cm}^{-3}$ and $1.8 \times 10^9 \text{ cm}^{-3}$, respectively (Zhang et al., 2022b).

213 Considering the system uncertainty and calibration uncertainty, the detection
214 limits of the OH and HO₂ radicals were $3.3 \times 10^5 \text{ cm}^{-3}$ and $1.1 \times 10^6 \text{ cm}^{-3}$ (60 s, 1σ),
215 respectively. At a typical laser power of 15 mW, the measurement accuracy for OH
216 and HO₂ measurement was 13% and 17%, respectively.

217 **2.2.2 Supporting measurements**

218 In addition to measuring the HO_x radicals, an extensive suite of relevant species
219 was also measured close to the LIF instrument to improve the analysis of the radical

220 photochemistry. Detailed information about the measurement instrument is presented
221 in Table S2, including the meteorological parameters (wind speed (WS), wind
222 direction (WD), temperature (T), relative humidity (RH), pressure (P), and solar
223 radiation (J-values)) and chemical parameters (ozone (O₃), carbon monoxide (CO),
224 sulfur dioxide (SO₂), HONO, NO, NO₂, HCHO, NMHCs, and particulate matter
225 (PM_{2.5})). HONO measurement was conducted using a commercial Long-Path
226 Absorption Photometer (LOPAP). The LOPAP method utilizes two absorption tubes
227 in series for differential correction, which effectively eliminates the influence of
228 known interfering substances such as NO₂ and N₂O₅, offering an advantage over
229 traditional wet chemistry methods. Zero air measurements were taken every 8 hours
230 for a duration of 20 minutes to correct for instrument baseline fluctuations. This
231 method has been extensively tested for its suitability in detecting HONO in complex
232 atmospheric conditions, as demonstrated in previous studies by (Yang et al., 2022a;
233 Yang et al., 2021b; Wang et al., 2023). Eight measured photolysis rates (j(NO₂),
234 j(H₂O₂), j(HCHO), j(HONO), j(NO₂), j(NO₃), j(O₁D)) were used as model constraints.
235 In addition to HCHO, other volatile organic compounds (VOCs) were detected using
236 a gas chromatograph coupled with a flame ionization detector and mass spectrometer
237 (GC-FID-MS). Ninety-nine types of VOCs, including C₂–C₁₁ alkanes, C₂–C₆ alkenes,
238 C₆–C₁₀ aromatics, halohydrocarbons, and some oxygenated VOCs (OVOCs), were
239 observed using the GC-FID-MS at a 1-h time interval. Only isoprene was considered
240 as a representative of biogenic VOCs (BVOCs). All of the instruments were located
241 close to the roof of the monitoring building, nearly 12 m above the ground to ensure
242 that all of the pollutants were located in a homogeneous air mass.

243 **2.3 Model description**

244 A 0-D chemical box model incorporating a condensed mechanism, the regional
245 atmospheric chemistry mechanism version 2-Leuven isoprene mechanism (RACM2-
246 LIM1), was used to simulate the radical concentrations and the generation of ozone
247 (Stockwell et al., 1997; Griffith et al., 2013; Tan et al., 2017). The meteorological
248 parameters, pollutants, and precursor concentrations mentioned in Section 2.2.2 were

249 input into the model as boundary conditions. All of the constraints were unified to a
 250 temporal resolution of 15 min through averaging or linear interpolation. The overall
 251 average during the observations was substituted for large areas of missing data due to
 252 instrument maintenance or failure. Three days of data were entered in advance as the
 253 spin-up period, and a synchronized time-dependent dataset was eventually generated.
 254 The hydrogen (H₂) and methane (CH₄) concentrations were set to fixed values of 550
 255 ppb and 1900 ppb, respectively. The physical losses of species due to processes such
 256 as deposition, convection, and advection were approximately replaced by an 18 h
 257 atmospheric lifetime, corresponding to first order loss rate of ~1.5 cm/s (by assuming
 258 a boundary layer height of about 1 km). The sensitivity analysis shows that when the
 259 lifetime changes within 8 – 24 hours, the values differed less than 5% for both OH,
 260 HO₂, *k*_{OH} (Fig. S4). According to the measurement accuracy, the simulation accuracy
 261 of the model for the OH and HO₂ radicals was 50% (Zhang et al., 2022a).

262 In addition, another steady-state calculation method (PSS) can also be used to
 263 estimate the concentrations of OH and HO₂ radicals (Eq. (1)(2), (Woodward-Massey
 264 et al., 2022a; Slater et al., 2020)). Since the *k*_{OH} and RO₂ concentrations were not
 265 obtained in this observation, simulated values are used as substitutes. Other radical
 266 and reactive intermediates are actual values that measured from the instruments in
 267 Table S2.

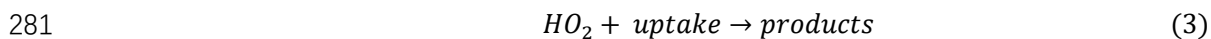
$$268 \quad [OH]_{PSS} = \frac{j_{HONO}[HONO] + \varphi_{OH}j(O^1D)[O_3] + k_{HO_2+NO}[NO][HO_2]}{k_{OH}} \quad (1)$$

$$269 \quad [HO_2]_{PSS} = \frac{k_{CO+OH}[CO][OH] + j_{HCHO}[HCHO] + k_{RO_2+NO}[NO][RO_2]}{k_{HO_2+NO}[NO]} \quad (2)$$

270 Considering the environmental characteristics of the MBL, the gas-phase
 271 mechanisms for bromine (Br) and iodine (I) were introduced into the base model to
 272 diagnose the impacts of the reactive bromine chemistry. The details of the
 273 mechanisms involved are listed in Tables S3 and S4. The halogen species were not
 274 available in the YMK site, so the typical levels of BrO and IO concentration in MBL
 275 site was used as a reference value (average daytime concentration of ~5 ppt) (Xia et
 276 al., 2022; Bloss et al., 2010; Whalley et al., 2010).

277 The heterogeneous uptake of HO₂ is considered to play an important role in the

278 MBL region (Whalley et al., 2010; Zou et al., 2022; Woodward-Massey et al., 2022a).
279 In order to assess the impact of HO₂ uptake on HO_x radical chemistry, we
280 incorporated HO₂ uptake reaction into the base model (Eq. (3) - (5)).



$$282 \quad k_{HO_2+uptake} = \frac{\gamma \times ASA \times v_{HO_2}}{k_{HO_2+NO}[NO]} \quad (4)$$

$$283 \quad v_{HO_2} = \sqrt{\frac{8 \times R \times T}{0.033 \times \Pi}} \quad (5)$$

284 Here, ASA represents the aerosol surface area [$\mu\text{m}^2 \text{cm}^{-3}$], which can be estimated
285 as 20 times the PM_{2.5} concentration [$\mu\text{g}/\text{cm}^3$]. v_{HO_2} [cm^{-1}] can be calculated using Eq.
286 (5), where T and R represent the temperature and gas constant, respectively. The
287 heterogeneous uptake coefficient (γ) for HO₂ usually has high uncertainty, with typical
288 values ranging from 0 to 1 (Song et al., 2021). In this study, we set γ to 0.08 to
289 evaluate the influence of HO₂ uptake on radical concentrations.

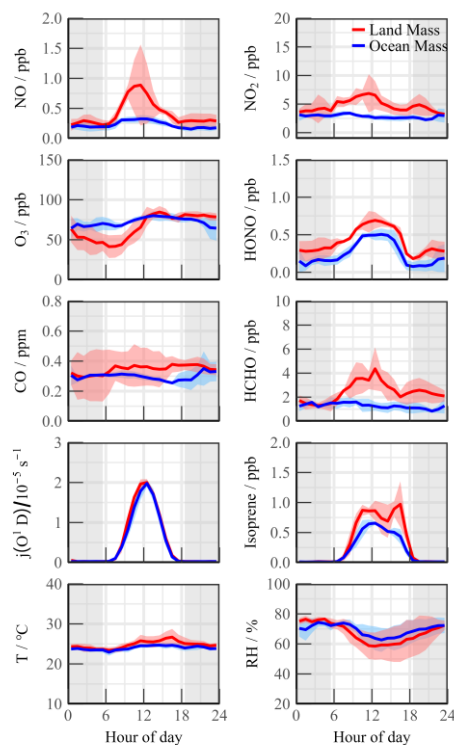
290 **3 Results**

291 **3.1 Meteorological and chemical parameters**

292 Fig. S3 presents the time series of the main meteorological parameters and
293 pollutants during the observation period at the YMK site. Except for on 2 days,
294 October 26 and 28, the meteorological characteristics of the other days were generally
295 stable. The daily maximum T, RH, and J-values did not vary significantly. The
296 suitable temperature (20–30°C) and humidity (40–80%) conditions promoted the
297 stable oxidation of the diurnal photochemistry. The peak $j(\text{O}^1\text{D})$ value was
298 approximately $2.0 \times 10^{-5} \text{ s}^{-1}$, exhibiting the typical characteristics of intense light
299 radiation in autumn in the Pearl River Delta region (Yang et al., 2022a; Tan et al.,
300 2022).

301 As typical marine air components, the concentrations of NO_x, CO, PM_{2.5}, and
302 other pollutants were lower than those detected in other observation campaigns in
303 both urban and suburban areas in the Pearl River Delta region (Tan et al., 2019b; Lu et
304 al., 2012; Yang et al., 2022b). Several observation campaigns have discovered the

305 relationship between wind direction and radical chemistry (Lu et al., 2012; Fuchs et
 306 al., 2017; Niu et al., 2022). Although there was no apparent wind speed condition, the
 307 dominant air mass still influenced the pollutant concentrations due to the particularity
 308 of the marine site.



309
 310 **Fig. 2.** Mean diurnal profiles of measured trace gases parameters during Land mass and Ocean mass episodes. The
 311 coloured shadows denote the 25 and 75% percentiles. The grey areas denote nighttime.

312 During the OCM period, the NO_x and HCHO concentrations exhibited relatively
 313 clean characteristics that were consistent with those previously observations in open
 314 ocean (RHAMBLe, SOS, CHABLIS and ALBATROSS, Table 1). Isoprene, a
 315 representative BVOC, achieved a diurnal concentration of 0.58 ± 0.06 ppb, indicated
 316 slightly local emissions could have impacted the concentrations of the precursor
 317 species even in OCM sector. The ozone concentration in the YMK site was always at
 318 the critical value of the updated Class I standard (GB3095-2012, average hourly O₃ of
 319 81 ppb at 25°C and 1013 kPa). The occurrence of fewer emissions reduced the
 320 titration effect, resulting in the ozone exhibiting no apparent diurnal trend on some of
 321 the dates and a high background value at night (78.1 ± 7.6 ppb).

322 As a coastal site, chemical conditions could be influenced by local land emissions
 323 depending on the wind direction. Compared with the OCM period, the meteorological

324 conditions (T, RH, and J-values) changed slightly during the LAM episode, but the
 325 pollutants were accumulated due to the transport of the plume from the northern cities
 326 (Fig. 2). The CO and PM_{2.5} concentrations exhibited good consistency and even mild
 327 pollution features ($(0.36 \pm 0.12 \text{ ppm})$ and $(37.70 \pm 7.91 \mu\text{g}/\text{m}^3)$, respectively),
 328 reflecting the influence of human activities. Both NO and NO₂ peaked at around
 329 10:00, exhibiting prominent pollution characteristics. HONO exhibited a distribution
 330 with high daytime ($0.66 \pm 0.08 \text{ ppb}$) and low nighttime ($0.33 \pm 0.09 \text{ ppb}$)
 331 concentrations. This unique distribution of HONO has been observed in remote
 332 environments in several previous observation campaigns (Jiang et al., 2022; Crilley et
 333 al., 2021). High HONO concentration in the daytime will affect the chemical
 334 composition of the atmosphere and the secondary pollution generation.

335 **Table 1.** Summary of radical concentrations and related species concentrations at MBL. All data are listed as the
 336 average in noontime (10:00~15:00).

Campaign	Location	Category	Date	OH (10 ⁶ cm ⁻³)	HO ₂ (10 ⁸ cm ⁻³)	HCHO (ppb)	HONO (ppb)	NO _x (ppb)	O ₃ (ppb)	Reference
WAOSE95	Weybourne, UK	Coastal	1995 (Jun)	5.0	-	1.50	0.10	<2.0	40.0	(Grenfell et al., 1999)
ALBATROSS	Atlantic Ocean	Open ocean	1996 (Oct-Nov)	7.0	-	0.50	-	-	25.0	(Brauers et al., 2001)
EASE96	Mace Head, Ireland	Coastal	1996 (Jul-Aug)	2.3	2.6	-	-	~1.0	45.0	(Carslaw et al., 1999)
EASE97	Mace Head, Ireland	Coastal	1997 (Apr-May)	1.8	1.0	0.70	-	0.95	46.0	(Creasey et al., 2002)
ORION99	Okinawa Island, Japan	Coastal	1999 (Aug)	4.0	4.3	-	0.20	6.3	23.0	(Kanaya et al., 2001)
RISOTTO	Rishiri Island, Japan	Coastal	2000 (June)	7.4	3.1	-	-	0.45	-	(Kanaya et al., 2002)
RISFEX	Rishiri Island, Japan	Coastal	2003 (Aug)	2.7	1.5	-	-	0.2	28.0	(Qi et al., 2007)
CHABLIS	Antarctica	Open ocean	2005 (Jan-Feb)	1.0	1.1	0.12	0.007	0.02	7.0	(Bloss et al., 2010)
RHaMBLe	Atlantic Ocean	Open ocean	2007 (May-Jun)	9.0	6.0	0.30	-	0.014	35.0	(Whalley et al., 2010)
SOS	Cape Verde, Atlantic Ocean	Open ocean	2009 (Jun; Sep)	9.0	4.0	1.9	-	0.050	40.0	(Carpenter et al., 2011)
CYPHEX	Cyprus, Mediterranean	Coastal	2014 (Jul)	5.8	6.3	~1.0	~0.080	<1.0	69.0	(Mallik et al., 2018)
ICOZA (NW-SE)	North Norfolk, UK	Coastal	2015 (Jul)	3.0	1.4	0.9	0.052	2.0	39.0	(Woodward-Massey et al., 2022a)
ICOZA (SW)	North Norfolk, UK	Coastal	2015 (Jul)	4.1	1.0	1.1	0.097	3.0	31.0	(Woodward-Massey et al., 2022a)
HT	Hok Tsui, China	Coastal	2020 (Oct-Nov)	4.9	-	1.0	0.15	~4.0	65.0	(Zou et al., 2022)
YMK (Land Mass)	Shenzhen, China	Coastal	2019 (Oct)	7.1	5.2	3.4	0.66	6.4	75.6	This work

YMK (Ocean Mass)	Shenzhen, China	Coastal	2019 (Oct)	4.5	4.9	1.2	0.48	3.0	78.1	This work
---------------------	--------------------	---------	---------------	-----	-----	-----	------	-----	------	-----------

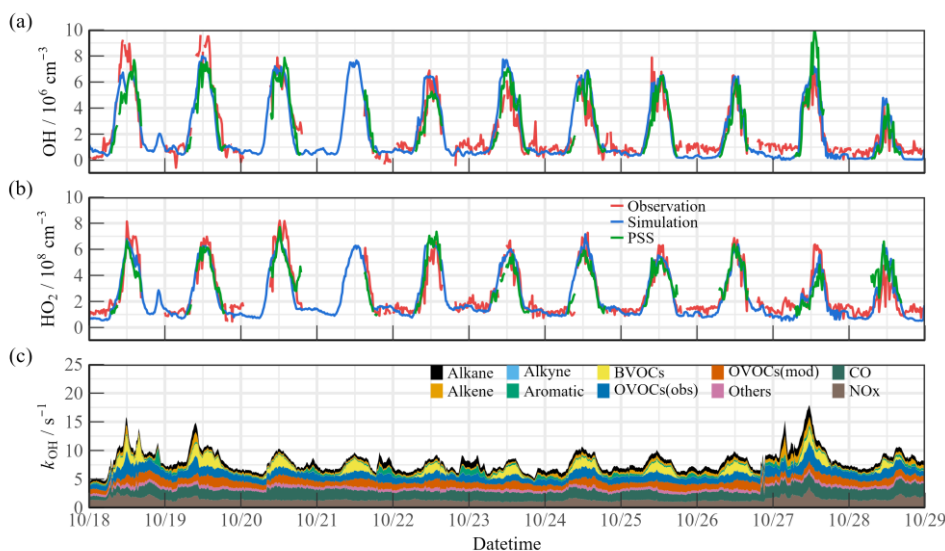
337

338 The detailed information for VOCs species during the YMK campaign has been
 339 added in the Table S5. The daily maximum NMHC concentration peaked at $27.81 \pm$
 340 9.91 ppb, and the maximum value of ~ 40 ppb occurred on October 27. Local
 341 biological emissions significantly affected the NMHC composition of the site, and
 342 isoprene achieved a noon maximum of 0.82 ± 0.16 ppb. Neither anthropogenic
 343 alkenes (2.21 ± 0.94 ppb) nor aromatic (1.31 ± 0.25 ppb) hydrocarbons were abundant,
 344 and OVOCs accounted for approximately 50% of the total. As a photochemical
 345 indicator, formaldehyde peaked at ~ 4 to ~ 8 ppb during the LAM episode, suggesting a
 346 more vigorous oxidation process. The HONO concentration was 6.8 times higher than
 347 the SW scenario in the ICOZA observation (a pollution period dominated by a
 348 southwest wind direction), while the HCHO concentration was 3.1 times higher.
 349 (Woodward-Massey et al., 2022a). The abundance of oxidation precursors (HONO,
 350 HCHO, O₃, and NMHCs) reflected the unique atmospheric conditions in the marine
 351 environment in China, which originated from the complex atmospheric pollution.

352 **3.2 HO_x radical concentrations and modeled OH reactivity**

353 Fig. 3(a)(b) shows the time series of the simulated and observed OH and HO₂
 354 radical concentrations during the observation campaign. The time series of the
 355 simulated OH reactivity (k_{OH}) is presented in Fig. 3(c). The observed OH and HO₂
 356 radicals exhibited significant diurnal trends. The daily maximum OH and HO₂ values
 357 were $(4.7\text{--}9.5) \times 10^6 \text{ cm}^{-3}$ and $(4.2\text{--}8.1) \times 10^8 \text{ cm}^{-3}$, respectively. The peak k_{OH} value
 358 was commonly less than 10 s^{-1} . Due to human activities, the simulated k_{OH} reached
 359 more than $\sim 15 \text{ s}^{-1}$ on some days. The radical concentrations and reactivity exhibited
 360 similar trends, which differed from reports on urban and semi-urban areas where
 361 inorganic species (NO_x and CO) were the dominant controllers of k_{OH} (Zhang et al.,
 362 2022a; Tan et al., 2019b; Lou et al., 2010). The k_{OVOCs} was separated into $k_{OVOCs(Obs)}$
 363 and $k_{OVOCs(Model)}$ (Fig. 3(c)). Specifically, $k_{OVOCs(Obs)}$ includes the observed species
 364 such as formaldehyde (HCHO), acetaldehyde (ACD), higher aldehydes (ALD),

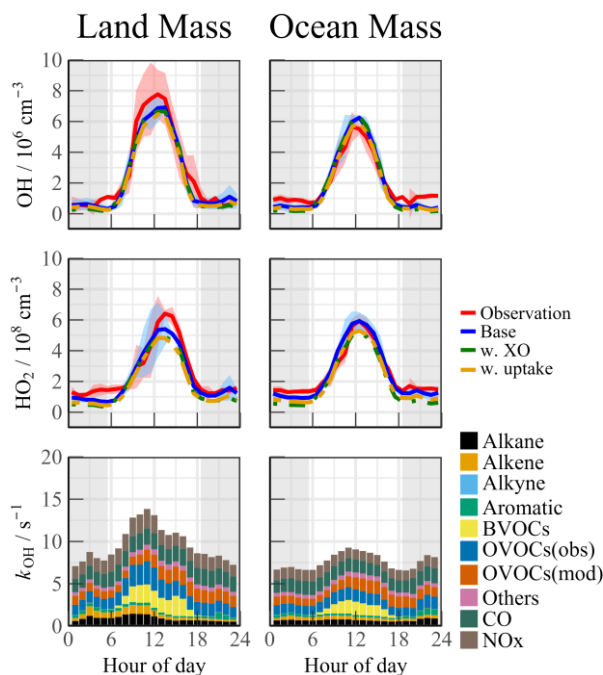
365 acetone (ACT), ketones (KET), and oxidation products of isoprene (MACR and
 366 MVK). The model-generated intermediates, such as glyoxal, methylglyoxal,
 367 methylethyl ketone, and methanol, are categorized as $k_{\text{OVOCs}(\text{Model})}$. Approximately 50%
 368 of the total k_{OVOCs} are represented by unconstrained species ($k_{\text{OVOCs}(\text{Model})}$), which
 369 contribute a daily k_{OH} of 1.39 s^{-1} . Overall, the observed OH and HO_2 concentrations
 370 were both well reproduced by the base model incorporating the RACM2-LIM1
 371 mechanism. The observed OH was underestimated only on the first days, and a slight
 372 model overestimation happened on October 23&24. PSS calculation showed good
 373 agreement with the base model, providing evidence of the balance of radical internal
 374 consistency in the daytime. It should be noted that the OH reactivity of unmeasured
 375 VOCs may be underestimated due to the lumped groups in RACM2 mechanism.



376
 377 **Fig. 3.** Timeseries of the observed and modelled parameters for OH, HO_2 and k_{OH} during the observation
 378 period. (a) OH, (b) HO_2 , (c) k_{OH} .

379 The air mass transport of the precursors induced photochemistry accumulation,
 380 which was then reflected in the changes in the oxidation progress. It is worth
 381 comparing the concentrations and reactivities of the radicals by classifying the
 382 predominant air mass (Fig. 4). During the OCM period, the observed OH and HO_2
 383 radicals could be reflected by the base chemical mechanism, with daily averages of
 384 $4.5 \times 10^6 \text{ cm}^{-3}$ and $4.9 \times 10^8 \text{ cm}^{-3}$, respectively. Compared to other campaigns (Table
 385 1), the observed maximum values were within reasonable ranges (OH: $2 - 9 \times 10^6$
 386 cm^{-3} ; HO_2 : $1 - 6 \times 10^8 \text{ cm}^{-3}$). Despite low NO_x levels during the OCM period, the

387 HO₂ radical was not overestimated using the base model, which was dissimilar to
388 many MBL observations (Bloss et al., 2010). However, both the OH and HO₂ radical
389 concentrations reached higher levels during the LAM-dominant period, indicating a
390 more active photochemical process (Section 4.1). The diel averages for the OH and
391 HO₂ radicals were $7.1 \times 10^6 \text{ cm}^{-3}$ and $5.2 \times 10^8 \text{ cm}^{-3}$, respectively, which were
392 notably higher than the levels reported in the ICOZA observations (Woodward-
393 Massey et al., 2022a). The base scenario underestimated both the OH and HO₂
394 concentrations between 10:00 and 15:00, and the observation-to-model ratio was
395 greater than 1.2. The calculated daily maximum total OH reactivity was 8.8 s^{-1} , and
396 nearly 70% of the reactivity was accounted for by the organic species, among which
397 the OVOCs were the largest contributor (30.6%). The anthropogenic alkanes, alkenes,
398 and aromatic hydrocarbons contributed less than 10% to the reactivity. Compared
399 with the OCM-dominant episode, the higher reactivity during the LAM period
400 indicated the occurrence of efficient recycling during the RO_x (the sum of OH, HO₂,
401 and RO₂) propagation (12.4 s^{-1} vs. 8.8 s^{-1}). The higher contributions of the BVOCs
402 (only isoprene was considered, 15.6%) and OVOCs (30.2%) to the reactivity reflected
403 the diverse composition of the VOCs in the forest environment. Under enhanced
404 photochemistry, the calculated OH reactivity could be an underestimation of the total
405 OH reactivity, so a missing OH source may be masked. As a representative of the
406 OVOCs, HCHO reflects the photochemical level to a certain extent. As shown in Fig.
407 S5, a solid positive dependence between the OH_{obs-to-OH_{mod}} ratio and HCHO was
408 observed (the daytime data were restricted according to $j(\text{O}^1\text{D}) > 5 \times 10^{-6} \text{ s}^{-1}$). With
409 the increase of photochemical intensity, the ratio between the observed and simulated
410 OH radical showed an obvious mismatch. Obtaining the full magnitude of the radical-
411 related parameters is necessary to compensate for the discrepancy in the concentration
412 closure experiments.



413

414

Fig. 4. Median diurnal profiles of the observed and modelled OH, HO₂, k_{OH} during LAM and OCM episodes. The coloured shadows for OH and HO₂ radicals denote the 25 and 75% percentiles. The grey areas denote nighttime.

415

416

417

418

419

420

421

422

423

424

425

426

427

428

429

430

431

432

Halogen species have been recognized as potent oxidizers that can boost photochemistry (Xia et al., 2022; Peng et al., 2021). A sensitivity test was performed by imposing BrO and IO into the base model to diagnose the impact of the halogen chemistry on the troposphere chemistry. The concentration of BrO and IO is set to ~5 ppt, which is a typical level in MBL site (Xia et al., 2022; Bloss et al., 2010; Whalley et al., 2010). The details of the mechanisms involved are listed in Tables S3 and S4. In this scenario (Fig. 4, green line). The daytime concentration of HO₂ radical decreased by 8.5% and 13.3% during the LAM and OCM periods, respectively, compared to the base model. However, there was no significant change in the concentration of OH radicals (<3%). Traditionally, it is believed that the inclusion of halogen chemistry leads to higher modeled OH concentrations and lower modeled HO₂ concentrations. Therefore, the lack of an increase in OH concentration with the introduction of the halogen mechanism at the YMK site calls for further investigation (Fig. S6). By modifying the NO concentration in different levels (Scenario 1: [NO] × 150%, Scenario 2: base, Scenario 3: [NO] × 20%, Scenario 4: [NO] × 10%), the response of HO_x radicals to the halogen mechanism varied under different NO levels. As the

433 constrained NO increased from 30 ppt to 500 ppt, the reduction in HO₂ radicals due to
434 the Br and I mechanisms ranged between 10% and 20%. At elevated NO_x levels,
435 reactions between halogen radicals and NO_x occurred, inhibiting the formation of OH
436 radicals. In Scenario 1, the OH concentration even decreased by 3.5% when
437 introducing the halogen mechanism. When NO concentration was constrained around
438 30 ppt (Scenario 4), similar to those obtained in RHaMBLe/CYPHEX campaigns, the
439 modelled OH concentration increased by 14.4%, while the HO₂ concentration
440 decreased by approximately 20.8% (Whalley et al., 2010; Bloss et al., 2010).
441 Therefore, the sensitivity of OH radicals to the halogen mechanism in the YMK
442 region is primarily limited by the local NO_x concentration level.

443 Although the modelled and measured HO₂ showed good agreement, the effect of
444 HO₂ heterogeneous processes on the chemistry of HO_x radicals is also worth
445 exploring. The inclusion of heterogeneous processes ($\gamma = 0.08$) did reduce the
446 modelled HO₂ concentration for ~10% during both LAM and OCM periods (Fig. 4,
447 yellow line). This reduced agreement between observation and simulation emphasizes
448 the presence of a missing HO₂ source in the base model.

449 **4 Discussion**

450 **4.1 Experimental radical budget balance**

451 **4.1.1 OH radical**

452 A process-oriented experiment was conducted to investigate the photochemistry
453 progress from a budget balance perspective (Woodward-Massey et al., 2022b; Tan et
454 al., 2019b; Yang et al., 2021a). The OH was in a photostationary steady state due to its
455 short lifetime. The total OH removal rate was directly quantified from the union of the
456 OH concentration and the reactivity (Eq.(6)):

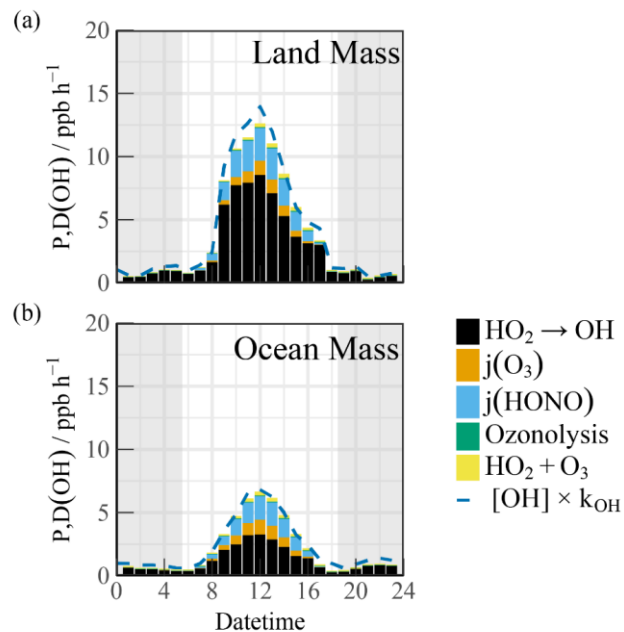
$$457 \quad D(OH) = [OH] \times k_{OH}. \quad (6)$$

458 The total production rate of the OH radical was the sum of the primary sources
459 (O₃/HONO photolysis and ozonolysis reactions) and secondary sources (HO₂ + NO)
460 (Eq.(7)):

$$\begin{aligned}
461 \quad P(OH) &= j_{HONO}[HONO] + \varphi_{OH}j(O^1D)[O_3] + \Sigma i \{ \varphi_{OH}^i k_{Alkenes+O_3}^i [Alkenes][O_3] \} \\
462 \quad &+ (k_{HO_2+NO}[NO] + k_{HO_2+O_3}[O_3])[HO_2]. \quad (7)
\end{aligned}$$

463 Here, φ_{OH} and φ_{OH}^i represent the OH yields in the O_3 photolysis and alkene
464 ozonolysis processes, respectively.

465 The diel profiles of the experimental OH budget during the LAM and OCM
466 periods are shown in Fig. 5. Both the observed OH and HO_2 radicals were introduced
467 into the budget calculations. Because k_{OH} was not measured during the observation
468 experiment, the simulated value was used to analyze the removal rate. Therefore,
469 $D(OH)$ should be considered a lower limit as it uses calculated rather than measured
470 k_{OH} (Yang et al., 2022b). During the OCM period, the $HO_2 + NO$ reaction accounted
471 for ~50% of the OH yield. The maximum of 6.6 ppb/h occurred at around 12:00. The
472 photolysis reactions could increase the daytime contributions of HONO and O_3 to
473 1.52 ppb/h and 0.84 ppb/h, respectively (10:00–15:00). The contribution of the non-
474 photolytic radical source (ozonolysis reactions) was almost negligible.



475 **Fig. 5.** The diurnal profiles of the experimental OH budget during (a) LAM and (b) OCM episodes. The blue
476 line denotes the OH destruction rate($[OH] \times k_{OH}$). The grey areas denote nighttime.
477

478 Compared with other marine observations, the calculated OH generation rate was
479 approximately twice that reported in the ICOZA and five times that obtained in the
480 RHAMBLE campaigns (Woodward-Massey et al., 2022b; Whalley et al., 2010).

481 During the LAM period, the OH generation rate reached a maximum of 12.6 ppb/h,
482 accompanied by a secondary source contribution of 67% (from the reaction between
483 HO₂ and NO) during the daytime, which was close to several observations related to
484 polluted plumes (Woodward-Massey et al., 2022b; Tan et al., 2019b; Lu et al., 2012;
485 Yang et al., 2022b). When the simulated k_{OH} was introduced into the experimental
486 budgets, the difference between P(OH) and D(OH) was less than 2 ppb/h.

487 **4.1.2 Total ROx radicals**

488 The budget analysis of the HO₂ and RO₂ radicals could not be performed well
489 due to the lack of RO₂ radical observation data. The diurnal profiles of the ROx
490 production (P(ROx)) and termination rate (L(ROx)) for the different air masses are
491 shown in Fig. 6. The P(ROx) could reach 3.36 ppb /h with an ocean plume. HONO
492 photolysis controlled nearly half of the primary sources (45.7%), and the daily
493 distribution was consistent with that of solar radiation. The ozone-related
494 contributions from photolysis and ozonolysis were approximately 46.6% (25.1% from
495 photolysis and 11.5% from ozonolysis, respectively). The remaining contribution was
496 from the photolysis of carbonyls (HCHO and OVOCs) (15.0%). The anthropogenic
497 contribution to the radical chemistry was not ignorable, and the ROx source in this
498 observation was exponentially higher than that in other MBL observations
499 (Woodward-Massey et al., 2022b; Stone et al., 2012; Whalley et al., 2010; Mallik et
500 al., 2018). The P(ROx) of the LAM was close to that in Shenzhen (~4 ppb/h) but was
501 significantly lower than that in Yufa (~7 ppb/h) and the BackGarden (~11 ppb/h) (Tan
502 et al., 2019b; Lu et al., 2012; Yang et al., 2022b). The reactions between ROx and
503 NOx and self-combination were the main pathways of radical termination (~70%).
504 The contribution of the formation of peroxyxynitrate to the L(ROx) could not be ignored
505 in the daytime.

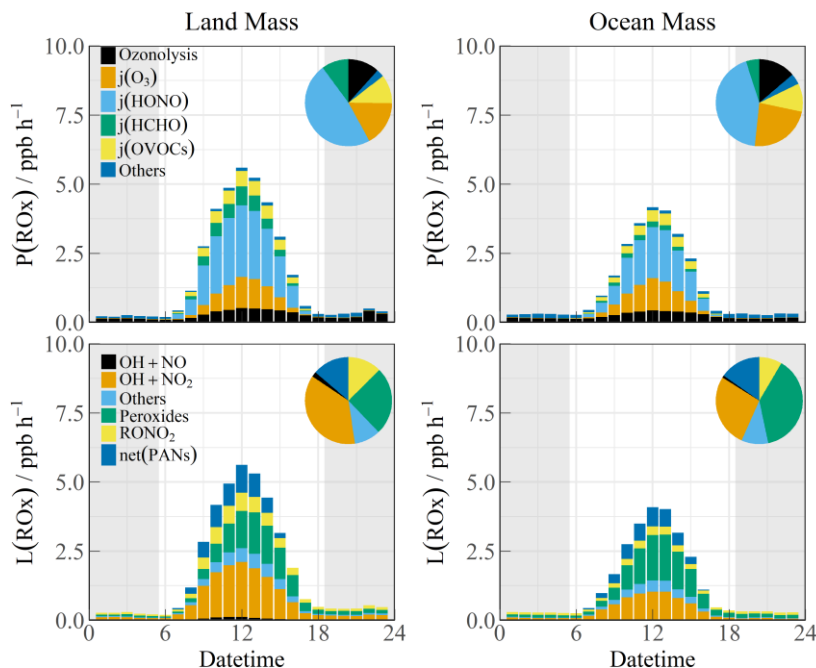


Fig. 6. The diurnal profiles of ROx budget during Land mass and Ocean mass episodes. The pie chart denotes proportions in different parts during the daytime (10:00-15:00). The grey areas denote nighttime.

506
507
508

509 The high daytime HONO concentrations observed at the YMK site is a notable
510 phenomenon. Due to the high HONO concentration during the daytime, the photolysis
511 reaction made daytime contributions of 1.52 ppb/h and 2.19 ppb/h during the OCM
512 and LAM periods, respectively. As the only known gas-phase source, OH + NO
513 accounted for a negligible proportion of the HONO production rate. Given the
514 location of the site, HONO from cruise ship emissions is a possible component of the
515 primary anthropogenic source (Sun et al., 2020). Other active tropospheric HONO
516 sources (heterogeneous reactions with NO₂ and $p(NO_3^-)$ photolysis) are worthy of
517 consideration and significantly contribute to the atmospheric oxidation in the MBL
518 area (Zhu et al., 2022; Crilley et al., 2021).

519 4.2 Local ozone production rate

520 Peroxy radical chemistry is the essential photochemical source of tropospheric
521 ozone (F(Ox), Eq.(8)):

$$522 \quad F(O_x) = k_{HO_2+NO}[NO][HO_2] + \sum_i (1 - \alpha_i) k_{RO_2^i+NO}[NO]RO_2^i \quad (8)$$

523 NO reacts with HO₂ and RO₂ radicals to form NO₂, and then, photolysis occurs to
524 form O₃ under solar radiation. NO₂ and ozone are the two sides of the oxidation
525 reservoir. The effect of local emissions on the photodynamic equilibrium can be
526 avoided by characterizing the photochemical production of the total oxidants (Tan et

527 al., 2019b). α_i represents the side generation ratio of organic nitrate, which also
 528 affects the quantum yield of NO_2 (Tan et al., 2018). O_x is mainly photochemically
 529 removed through ozone photolysis, ozonolysis, radical chain propagation ($\text{OH}/\text{HO}_2 +$
 530 O_3), and chain termination ($\text{OH} + \text{NO}_2$) reactions in the troposphere ($D(\text{O}_x)$, Eq.(9)):

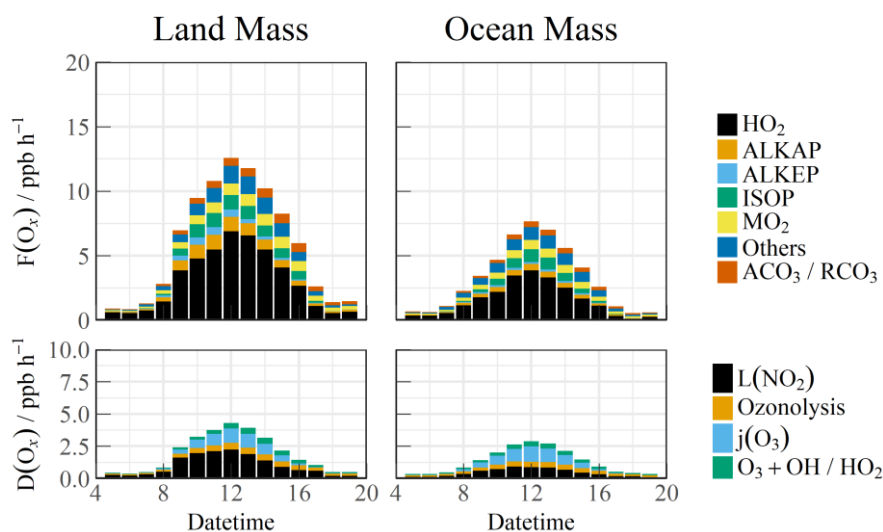
$$D(\text{O}_x) = \varphi_{\text{OH}} j(\text{O}^1\text{D})[\text{O}_3] + \sum_i \{k_{\text{Alkenes}+\text{O}_3}^i [\text{Alkenes}][\text{O}_3]\} + (k_{\text{O}_3+\text{OH}}[\text{OH}] +$$

$$k_{\text{O}_3+\text{HO}_2}[\text{HO}_2])[\text{O}_3] + k_{\text{OH}+\text{NO}_2}[\text{OH}][\text{NO}_2] \quad (9)$$

533 The net formation rate $P(\text{O}_x)$ can be calculated by subtracting $D(\text{O}_x)$ from $F(\text{O}_x)$
 534 (Eq.(10)):

$$P(\text{O}_x) = F(\text{O}_x) - D(\text{O}_x) \quad (10)$$

536 The simulated RO_2 radical concentration was introduced into the $F(\text{O}_x)$
 537 calculation. The diurnal variations in the ozone generation in the different air masses
 538 are shown in Fig. 7. The contribution of the HO_2 radical to $F(\text{O}_x)$ was approximately
 539 60%. The RO_2 radicals consisted of various types such as methyl peroxy (MO_2),
 540 acetyl peroxy radicals ($\text{ACO}_3/\text{RCO}_3$), and other radicals derived from alkanes
 541 (ALKAP), alkenes (ALKEP), and isoprene (ISOP), which accounted for an additional
 542 40% of the $F(\text{O}_x)$. On a daytime basis, the maximum $F(\text{O}_x)$ reached 7.4 ppb/h at
 543 around 12:00 in the OCM period, while a persistent-high value (maximum of 12.5
 544 ppb/h at 10:00–14:00) occurred in the LAM period. A vast amount of O_x was
 545 consumed in the nitric acid ($\text{OH} + \text{NO}_2$) formation pathways, i.e., higher than the
 546 ozonolysis removal. The daily averaged ozone production rates were 5.52 and 2.76
 547 ppb/h during the LAM and OCM periods, respectively.



548

549

550

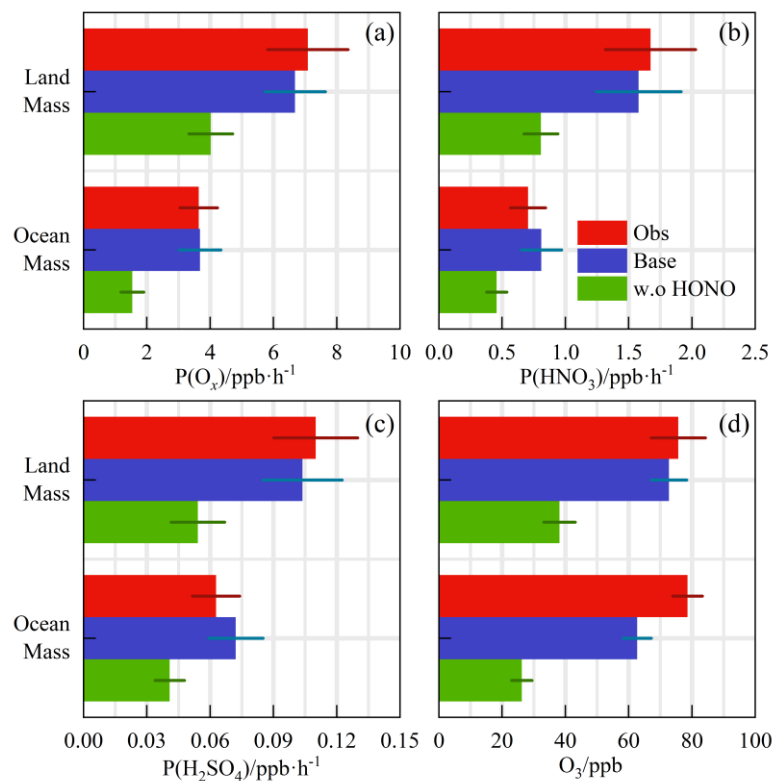
Fig. 7. The diurnal profiles of the speciation $F(\text{O}_x)$ and $D(\text{O}_x)$ during Land mass and Ocean mass episodes. The data were calculated by the measured OH and HO_2 and modelled RO_2 radicals.

551 **4.3 Relationship between precursors and oxidation rates**

552 Despite the low level of human activities, oxidation precursors have an extended
553 lifetime in the stable atmosphere of coastal areas. Intensive photochemical reactions
554 occur after the accumulation of precursors, resulting in local net ozone production
555 comparable to that in the surrounding suburban environments (Zeren et al., 2022).
556 Simultaneous observations of both urban and coastal settings in Shenzhen have
557 indicated that the oxidation rates are comparable (Xia et al., 2021). The coupling of
558 precursor transport and local photochemical processes in marine areas makes it
559 meaningful to explore secondary pollution generation (Fig. 8(a), (b), and (c)). No
560 obvious radical source was missing during the LAM and OCM periods, and the
561 oxidation level was that expected from the base model. On a daytime basis, the mean
562 diurnal profile of the P(Ox) reached ~ 7 ppb/h in the LAM period, and the average
563 nitric acid (P(HNO₃)) and sulfuric acid (P(H₂SO₄)) production rates were ~ 1.6 and
564 ~ 0.11 ppb/h, respectively. The P(HNO₃) production rate was similar to the average of
565 observations in the Pearl River Delta region (~ 1.3 ppb/h), while that of the P(H₂SO₄)
566 was only half the average level (~ 0.24 ppb/h) (Lu et al., 2013; Tan et al., 2019b; Yang
567 et al., 2022b). During the OCM period, the characteristics of the ocean air mass
568 alleviated the photochemical process, and the production rates of the secondary
569 pollutants decreased by approximately half and were close to the average levels in
570 winter (Ma et al., 2019).

571 Contrary to numerous ocean observations, in the YMK site, intensive oxidation
572 was accompanied by a high diurnal HONO level (higher than 400 ppt) (Fig. 9). The
573 ozone levels were consistent with the Grade I air quality standard and far exceeded
574 the global background concentration (~ 40 ppb). Daytime photolysis reactions of
575 HONO contributed 1.52 ppb/h and 2.19 ppb/h to P(ROx) during the OCM and LAM
576 periods, respectively, which were much higher than the values in several megacities
577 during the photochemically polluted season (Tan et al., 2019a). Given the significance
578 of HONO photolysis in driving atmospheric chemistry, a sensitivity test was
579 conducted without constraints on HONO (i.e., w.o HONO) to specifically quantify the

580 contribution of HONO-induced secondary pollution. Only the homogeneous reaction
 581 (OH + NO) participated in the formation of HONO in the default mode without
 582 HONO input (Liu et al., 2022b).



583

584 **Fig. 8.** The calculated reaction rates based on the observed concentrations for Land mass and Ocean mass
 585 episodes (a) P(Ox), (b) P(HNO₃), (c) P(H₂SO₄). (d) The observed and modelled O₃ concentration with a first-order
 586 loss term. The deposition process was equivalent to a lifetime of 15 hours to all species. All the rates and
 587 concentration are averaged for the daytime period between 10:00 and 15:00.

588 The modelled OH, HO₂ and RO₂ change when the model was unconstrained to
 589 HONO were shown in Fig. S7. After evaluation, in LAM and OCM sectors,
 590 concentration changes for OH were 46.9% and 43.2%, for HO₂ were 38.3% and
 591 34.3%, for RO₂ were 43.7% and 39.0%, respectively. The P(Ox) was found to be 33%
 592 and 39% lower during the LAM and OCM periods, respectively. The nitric acid
 593 (P(HNO₃)) and sulfuric acid (P(H₂SO₄)) formation rates also increased
 594 simultaneously (~43% and ~48% for LAM and OCM sectors, respectively). The
 595 sensitivity test identified the privileged role of the HONO-related mechanisms in the
 596 OH chemistry, which resulted in a correlation between the efficient radical recycling
 597 and secondary pollution.

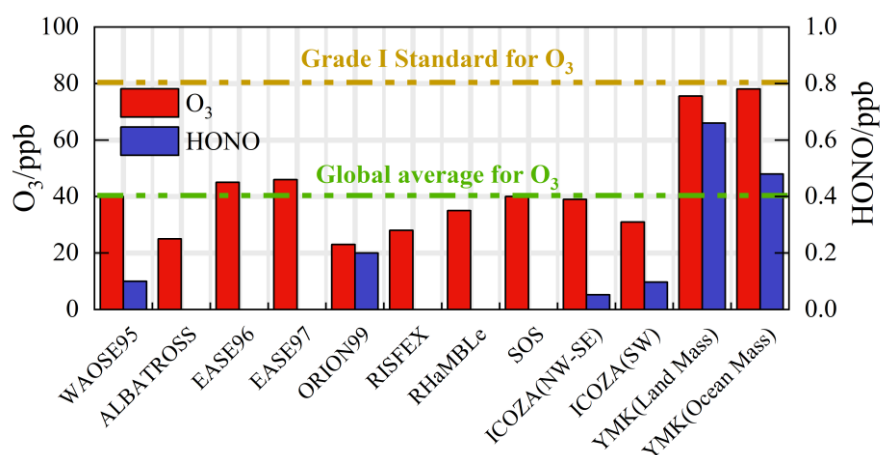


Fig. 9. Summary of both ozone and HONO concentrations in previous marine observations. The concentrations are averaged for the daytime period between 10:00 and 15:00.

598
599
600

601 A time-dependent box model was used to test the association between the HONO
602 chemistry and the local ozone generation (Fig. 8(d)). In order to isolate the O₃
603 photochemical production, the impacts of vertical entrainment and horizontal
604 advection were in general ignored. On the basis of the base scenario run, constraints
605 of the observed ozone and NO concentrations were removed to predict ozone. The
606 observed and modelled O₃ concentrations in Fig. 8(d) are averaged for the daytime
607 period between 10:00 and 15:00. The observed diurnal ozone concentrations were
608 75.7 ppb and 78.6 ppb during the LAM and OCM periods, respectively. The daytime
609 ozone was well reproduced by the time-dependent box model, and the deviation of the
610 simulation was less than 20% (Fig. 8(d)). After removing the HONO constraint, the
611 simulated ozone concentrations were 38.2 and 26.3 ppb, i.e., 48% and 58% lower,
612 during the LAM and OCM periods, respectively. Simulated O₃ decreased from ~75
613 ppb to a global background, and daytime HONO concentration were reduced to a low
614 level (~70 ppt) (Woodward-Massey et al., 2022a; Zhu et al., 2022; Xia et al., 2022).
615 The elevated daytime HONO had an additional effect on the oxidation in the
616 background atmosphere. For coastal cities, the particularity of the HONO chemistry
617 in the MBL tends to influence the ozone-sensitive system and eventually magnifies
618 the ozone background. Therefore, the promotion of oxidation by elevated precursor
619 concentrations is worth considering when formulating emission reduction policies. In
620 regions where HONO concentrations are elevated, the sources of HONO would need
621 to be identified to aid pollution mitigation policies.

5 Conclusions

Comprehensive observations of HOx radicals and other relevant species were conducted in October 2019 at a coastal site in the Pearl River Delta (the YMK site, 22.55°N, 114.60°E). The overall air pollutants exhibited typical coastal features due to the scarce anthropogenic emissions. The daily maximum OH and HO₂ concentrations were $(4.7\text{--}9.5) \times 10^6 \text{ cm}^{-3}$ and $(4.2\text{--}8.1) \times 10^8 \text{ cm}^{-3}$, respectively. The base RACM2-LIM1 model satisfactorily reproduced both the observed OH and HO₂ radical concentrations, but a slight overestimation of the OH radical occurred. The daily maximum calculated total OH reactivity was 9.9 s^{-1} , and nearly 70% of the reactivity was contributed by organic species.

In addition to anthropogenic and vegetation emissions, the synchronized air mass transport from the northern cities and the South China Sea exerted a time-varying influence on radical photochemistry and atmospheric oxidation. During the OCM period, the observed OH and HO₂ radical concentrations could be reflected by the base chemical mechanism, with daily average values of $4.5 \times 10^6 \text{ cm}^{-3}$ and $4.9 \times 10^8 \text{ cm}^{-3}$, respectively.

In the episode that was dominated by ocean mass, the HO₂ + NO reaction accounted for ~50% of the primary OH yield. A higher OH generation rate was found (12.6 ppb/h) during the LAM period, and the secondary source accounted for 67% of the total, which was similar to several observations in polluted plumes. Reactions between ROx and NOx and self-combination were the main pathways of radical termination (~70%), and the contribution of peroxyxynitrate formation to the L(ROx) could not be ignored in the daytime.

Intensive photochemical reactions occur after the accumulation of precursors, resulting in local net ozone production comparable to that in the surrounding suburban environments. The daily average ozone production rates were 5.52 and 2.76 ppb/h in the LAM and OCM periods, respectively. The rapid oxidation process was accompanied by a higher diurnal HONO concentration (higher than 400 ppt). A non-HONO-constrained sensitivity test was performed to quantify the HONO-induced

651 contribution to secondary pollution. After evaluation, the P(Ox) values were 33% and
652 39% lower during the LAM and OCM periods, respectively. The nitric acid (P(HNO₃))
653 and sulfuric acid (P(H₂SO₄)) formation rates also increased simultaneously (~43%
654 and ~48% for LAM and OCM sectors, respectively). Simulated O₃ decreased from
655 ~75 ppb to a global background, and daytime HONO concentration were reduced to a
656 low level (~70 ppt). For coastal cities, the particularity of the HONO chemistry in the
657 MBL tends to influence the ozone-sensitive system and eventually magnifies the
658 ozone background. Therefore, the promotion of oxidation by elevated precursor
659 concentrations is worth considering when formulating emission reduction policies.

660 **Financial support**

661 This work was supported by the National Natural Science Foundation of China
662 (62275250, U19A2044, 61905003), the Natural Science Foundation of Anhui
663 Province (No. 2008085J20), the National Key R&D Program of China
664 (2022YFC3700301), and the Anhui Provincial Key R&D Program (2022107020022).

665 **Data availability**

666 The data used in this study are available from the corresponding author upon request
667 (rzhu@aiofm.ac.cn).

668 **Author contributions**

669 WQ Liu, PH Xie, RZ Hu contributed to the conception of this study. GX Zhang and
670 RZ Hu performed the data analyses and manuscript writing. All authors contributed to
671 measurements, discussed results, and commented on the paper.

672 **Competing interests**

673 The contact author has declared that none of the authors has any competing interests.
674
675

References

- 677 Bloss, W. J., Camredon, M., Lee, J. D., Heard, D. E., Plane, J. M. C., Saiz-Lopez, A., Bauguutte, S. J. B.,
678 Salmon, R. A., and Jones, A. E.: Coupling of HO_x, NO_x and halogen chemistry in the antarctic
679 boundary layer, *Atmos Chem Phys*, 10, 10187-10209, 10.5194/acp-10-10187-2010, 2010.
- 680 Brauers, T., Hausmann, M., Bister, A., Kraus, A., and Dorn, H.-P.: OH radicals in the boundary layer of
681 the Atlantic Ocean: 1. Measurements by long-path laser absorption spectroscopy, *Journal of*
682 *Geophysical Research*, 106, 7399, 10.1029/2000jd900679, 2001.
- 683 Carpenter, L. J., Fleming, Z. L., Read, K. A., Lee, J. D., Moller, S. J., Hopkins, J. R., Purvis, R. M.,
684 Lewis, A. C., Müller, K., Heinold, B., Herrmann, H., Fomba, K. W., van Pinxteren, D., Müller, C.,
685 Tegen, I., Wiedensohler, A., Müller, T., Niedermeier, N., Achterberg, E. P., Patey, M. D., Kozlova, E. A.,
686 Heimann, M., Heard, D. E., Plane, J. M. C., Mahajan, A., Oetjen, H., Ingham, T., Stone, D., Whalley, L.
687 K., Evans, M. J., Pilling, M. J., Leigh, R. J., Monks, P. S., Karunaharan, A., Vaughan, S., Arnold, S. R.,
688 Tschritter, J., Pöhler, D., Friß, U., Holla, R., Mendes, L. M., Lopez, H., Faria, B., Manning, A. J., and
689 Wallace, D. W. R.: Seasonal characteristics of tropical marine boundary layer air measured at the Cape
690 Verde Atmospheric Observatory, *J Atmos Chem*, 67, 87-140, 10.1007/s10874-011-9206-1, 2011.
- 691 Carslaw, N., Creasey, D. J., Heard, D. E., Lewis, A. C., McQuaid, J. B., Pilling, M. J., Monks, P. S.,
692 Bandy, B. J., and Penkett, S. A.: Modeling OH, HO₂, and RO₂radicals in the marine boundary layer: 1.
693 Model construction and comparison with field measurements, *Journal of Geophysical Research:*
694 *Atmospheres*, 104, 30241-30255, 10.1029/1999jd900783, 1999.
- 695 Chen, W., Guenther, A. B., Shao, M., Yuan, B., Jia, S., Mao, J., Yan, F., Krishnan, P., and Wang, X.:
696 Assessment of background ozone concentrations in China and implications for using region-specific
697 volatile organic compounds emission abatement to mitigate air pollution, *Environ Pollut*, 305, 119254,
698 10.1016/j.envpol.2022.119254, 2022.
- 699 Creasey, D. J., Heard, D. E., and Lee, J. D.: Eastern Atlantic Spring Experiment 1997 (EASE97) 1.
700 Measurements of OH and HO₂ concentrations at Mace Head, Ireland, *Journal of Geophysical Research:*
701 *Atmospheres*, 107, ACH 3-1-ACH 3-15, 10.1029/2001jd000892, 2002.
- 702 Crilley, L. R., Kramer, L. J., Pope, F. D., Reed, C., Lee, J. D., Carpenter, L. J., Hollis, L. D. J., Ball, S.
703 M., and Bloss, W. J.: Is the ocean surface a source of nitrous acid (HONO) in the marine boundary
704 layer?, *Atmos Chem Phys*, 21, 18213-18225, 10.5194/acp-21-18213-2021, 2021.
- 705 Fuchs, H., Dorn, H. P., Bachner, M., Bohn, B., Brauers, T., Gomm, S., Hofzumahaus, A., Holland, F.,
706 Nehr, S., Rohrer, F., Tillmann, R., and Wahner, A.: Comparison of OH concentration measurements by
707 DOAS and LIF during SAPHIR chamber experiments at high OH reactivity and low NO concentration,
708 *Atmos Meas Tech*, 5, 1611-1626, 10.5194/amt-5-1611-2012, 2012.
- 709 Fuchs, H., Tan, Z., Lu, K., Bohn, B., Broch, S., Brown, S. S., Dong, H., Gomm, S., Haeseler, R., He, L.,
710 Hofzumahaus, A., Holland, F., Li, X., Liu, Y., Lu, S., Min, K.-E., Rohrer, F., Shao, M., Wang, B., Wang,
711 M., Wu, Y., Zeng, L., Zhang, Y., Wahner, A., and Zhang, Y.: OH reactivity at a rural site (Wangdu) in
712 the North China Plain: contributions from OH reactants and experimental OH budget, *Atmos Chem*
713 *Phys*, 17, 645-661, 10.5194/acp-17-645-2017, 2017.
- 714 Grenfell, J. L., Savage, N. H., Harrison, R. M., Penkett, S. A., Forberich, O., Comes, F. J., Clemitshaw,
715 K. C., Burgess, R. A., Cardenas, L. M., Davison, B., and McFadyen, G. G.: Tropospheric box-
716 modelling and analytical studies of the hydroxyl (OH) radical and related species: Comparison with
717 observations, *J Atmos Chem*, 33, 183-214, 10.1023/a:1006009901180, 1999.

718 Griffith, S. M., Hansen, R. F., Dusanter, S., Stevens, P. S., Alaghmand, M., Bertman, S. B., Carroll, M.
719 A., Erickson, M., Galloway, M., Grossberg, N., Hottle, J., Hou, J., Jobson, B. T., Kammrath, A.,
720 Keutsch, F. N., Lefer, B. L., Mielke, L. H., O'Brien, A., Shepson, P. B., Thurlow, M., Wallace, W.,
721 Zhang, N., and Zhou, X. L.: OH and HO₂ radical chemistry during PROPHET 2008 and CABINEX
722 2009-Part 1: Measurements and model comparison, *Atmos Chem Phys*, 13, 5403-5423, 10.5194/acp-
723 13-5403-2013, 2013.

724 Huang, R. J., Hoffmann, T., Ovadnevaite, J., Laaksonen, A., Kokkola, H., Xu, W., Xu, W., Ceburnis, D.,
725 Zhang, R., Seinfeld, J. H., and O'Dowd, C.: Heterogeneous iodine-organic chemistry fast-tracks marine
726 new particle formation, *Proc Natl Acad Sci U S A*, 119, e2201729119, 10.1073/pnas.2201729119, 2022.

727 Jiang, Y., Xue, L., Shen, H., Dong, C., Xiao, Z., and Wang, W.: Dominant Processes of HONO Derived
728 from Multiple Field Observations in Contrasting Environments, *Environmental Science & Technology*
729 *Letters*, 10.1021/acs.estlett.2c00004, 2022.

730 Kanaya, Y., Sadanaga, Y., Nakamura, K., and Akimoto, H.: Behavior of OH and HO₂ radicals during
731 the Observations at a Remote Island of Okinawa (ORION99) field campaign 1. Observation using a
732 laser-induced fluorescence instrument, *J Geophys Res-Atmos*, 106, 24197-24208,
733 10.1029/2000jd000178, 2001.

734 Kanaya, Y., Yokouchi, Y., Matsumoto, J., Nakamura, K., Kato, S., Tanimoto, H., Furutani, H., Toyota,
735 K., and Akimoto, H.: Implications of iodine chemistry for daytime HO₂ levels at Rishiri Island,
736 *Geophys Res Lett*, 29, 45-41-45-44, 10.1029/2001gl014061, 2002.

737 Liu, C., Liu, G., Casazza, M., Yan, N., Xu, L., Hao, Y., Franzese, P. P., and Yang, Z.: Current Status and
738 Potential Assessment of China's Ocean Carbon Sinks, *Environ Sci Technol*, 56, 6584-6595,
739 10.1021/acs.est.1c08106, 2022a.

740 Liu, P., Xue, C., Ye, C., Liu, C., Zhang, C., Wang, J., Zhang, Y., Liu, J., and Mu, Y.: The Lack of
741 HONO Measurement May Affect the Accurate Diagnosis of Ozone Production Sensitivity, *ACS*
742 *Environmental Au*, 10.1021/acsenvironau.2c00048, 2022b.

743 Liu, T., Hong, Y., Li, M., Xu, L., Chen, J., Bian, Y., Yang, C., Dan, Y., Zhang, Y., Xue, L., Zhao, M.,
744 Huang, Z., and Wang, H.: Atmospheric oxidation capacity and ozone pollution mechanism in a coastal
745 city of southeastern China: analysis of a typical photochemical episode by an observation-based model,
746 *Atmos Chem Phys*, 22, 2173-2190, 10.5194/acp-22-2173-2022, 2022c.

747 Lou, S., Holland, F., Rohrer, F., Lu, K., Bohn, B., Brauers, T., Chang, C. C., Fuchs, H., Haseler, R.,
748 Kita, K., Kondo, Y., Li, X., Shao, M., Zeng, L., Wahner, A., Zhang, Y., Wang, W., and Hofzumahaus, A.:
749 Atmospheric OH reactivities in the Pearl River Delta – China in summer 2006: measurement and
750 model results, *Atmos Chem Phys*, 10, 11243–11260, 10.5194/acp-10-11243-2010, 2010.

751 Lu, K. D., Guo, S., Tan, Z. F., Wang, H. C., Shang, D. J., Liu, Y. H., Li, X., Wu, Z. J., Hu, M., and
752 Zhang, Y. H.: Exploring atmospheric free-radical chemistry in China: the self-cleansing capacity and
753 the formation of secondary air pollution, *Natl. Sci. Rev.*, 6, 579-594, 10.1093/nsr/nwy073, 2019.

754 Lu, K. D., Hofzumahaus, A., Holland, F., Bohn, B., Brauers, T., Fuchs, H., Hu, M., Haeseler, R., Kita,
755 K., Kondo, Y., Li, X., Lou, S. R., Oebel, A., Shao, M., Zeng, L. M., Wahner, A., Zhu, T., Zhang, Y. H.,
756 and Rohrer, F.: Missing OH source in a suburban environment near Beijing: observed and modelled
757 OH and HO₂ concentrations in summer 2006, *Atmos Chem Phys*, 13, 1057-1080, 10.5194/acp-13-
758 1057-2013, 2013.

759 Lu, K. D., Rohrer, F., Holland, F., Fuchs, H., Bohn, B., Brauers, T., Chang, C. C., Haeseler, R., Hu, M.,
760 Kita, K., Kondo, Y., Li, X., Lou, S. R., Nehr, S., Shao, M., Zeng, L. M., Wahner, A., Zhang, Y. H., and
761 Hofzumahaus, A.: Observation and modelling of OH and HO₂ concentrations in the Pearl River Delta

762 2006: a missing OH source in a VOC rich atmosphere, *Atmos Chem Phys*, 12, 1541-1569,
763 10.5194/acp-12-1541-2012, 2012.

764 Ma, X. F., Tan, Z. F., Lu, K. D., Yang, X. P., Liu, Y. H., Li, S. L., Li, X., Chen, S. Y., Novelli, A., Cho,
765 C. M., Zeng, L. M., Wahner, A., and Zhang, Y. H.: Winter photochemistry in Beijing: Observation and
766 model simulation of OH and HO₂ radicals at an urban site, *Sci Total Environ*, 685, 85-95,
767 10.1016/j.scitotenv.2019.05.329, 2019.

768 Mallik, C., Tomsche, L., Bourtsoukidis, E., Crowley, J. N., Derstroff, B., Fischer, H., Hafermann, S.,
769 Hüser, I., Javed, U., Keßel, S., Lelieveld, J., Martinez, M., Meusel, H., Novelli, A., Phillips, G. J.,
770 Pozzer, A., Reiffs, A., Sander, R., Taraborrelli, D., Sauvage, C., Schuladen, J., Su, H., Williams, J., and
771 Harder, H.: Oxidation processes in the eastern Mediterranean atmosphere: evidence from the modelling
772 of HO_x; measurements over Cyprus, *Atmos Chem Phys*, 18, 10825-10847, 10.5194/acp-18-10825-
773 2018, 2018.

774 Niu, Y. B., Zhu, B., He, L. Y., Wang, Z., Lin, X. Y., Tang, M. X., and Huang, X. F.: Fast Nocturnal
775 Heterogeneous Chemistry in a Coastal Background Atmosphere and Its Implications for Daytime
776 Photochemistry, *Journal of Geophysical Research: Atmospheres*, 127, 10.1029/2022jd036716, 2022.

777 Peng, X., Wang, W. H., Xia, M., Chen, H., Ravishankara, A. R., Li, Q. Y., Saiz-Lopez, A., Liu, P. F.,
778 Zhang, F., Zhang, C. L., Xue, L. K., Wang, X. F., George, C., Wang, J. H., Mu, Y. J., Chen, J. M., and
779 Wang, T.: An unexpected large continental source of reactive bromine and chlorine with significant
780 impact on wintertime air quality, *Natl. Sci. Rev.*, 8, 10.1093/nsr/nwaa304, 2021.

781 Qi, B., Kanaya, Y., Takami, A., Hatakeyama, S., Kato, S., Sadanaga, Y., Tanimoto, H., and Kajii, Y.:
782 Diurnal peroxy radical chemistry at a remote coastal site over the sea of Japan, *Journal of Geophysical*
783 *Research*, 112, 10.1029/2006jd008236, 2007.

784 Slater, E. J., Whalley, L. K., Woodward-Massey, R., Ye, C., Lee, J. D., Squires, F., Hopkins, J. R.,
785 Dunmore, R. E., Shaw, M., Hamilton, J. F., Lewis, A. C., Crilley, L. R., Kramer, L., Bloss, W., Vu, T.,
786 Sun, Y., Xu, W., Yue, S., Ren, L., Acton, W. J. F., Hewitt, C. N., Wang, X., Fu, P., and Heard, D. E.:
787 Elevated levels of OH observed in haze events during wintertime in central Beijing, *Atmos Chem Phys*,
788 20, 14847-14871, 10.5194/acp-20-14847-2020, 2020.

789 Song, H., Lu, K., Dong, H., Tan, Z., Chen, S., Zeng, L., and Zhang, Y.: Reduced Aerosol Uptake of
790 Hydroperoxyl Radical May Increase the Sensitivity of Ozone Production to Volatile Organic
791 Compounds, *Environmental Science & Technology Letters*, 9, 22-29, 10.1021/acs.estlett.1c00893,
792 2021.

793 Stockwell, W. R., Kirchner, F., Kuhn, M., and Seefeld, S.: A new mechanism for regional atmospheric
794 chemistry modeling, *J Geophys Res-Atmos*, 102, 25847-25879, 10.1029/97jd00849, 1997.

795 Stone, D., Whalley, L. K., and Heard, D. E.: Tropospheric OH and HO₂ radicals: field measurements
796 and model comparisons, *Chemical Society reviews*, 41, 6348-6404, 10.1039/c2cs35140d, 2012.

797 Sun, L., Chen, T., Jiang, Y., Zhou, Y., Sheng, L., Lin, J., Li, J., Dong, C., Wang, C., Wang, X., Zhang,
798 Q., Wang, W., and Xue, L.: Ship emission of nitrous acid (HONO) and its impacts on the marine
799 atmospheric oxidation chemistry, *Sci Total Environ*, 735, 139355, 10.1016/j.scitotenv.2020.139355,
800 2020.

801 Tan, Z., Lu, K., Ma, X., Chen, S., He, L., Huang, X., Li, X., Lin, X., Tang, M., Yu, D., Wahner, A., and
802 Zhang, Y.: Multiple Impacts of Aerosols on O(3) Production Are Largely Compensated: A Case Study
803 Shenzhen, China, *Environ Sci Technol*, 10.1021/acs.est.2c06217, 2022.

804 Tan, Z., Lu, K., Jiang, M., Su, R., Wang, H., Lou, S., Fu, Q., Zhai, C., Tan, Q., Yue, D., Chen, D., Wang,
805 Z., Xie, S., Zeng, L., and Zhang, Y.: Daytime atmospheric oxidation capacity in four Chinese

806 megacities during the photochemically polluted season: a case study based on box model simulation,
807 *Atmos Chem Phys*, 19, 3493-3513, 10.5194/acp-19-3493-2019, 2019a.

808 Tan, Z. F., Lu, K. D., Dong, H. B., Hu, M., Li, X., Liu, Y. H., Lu, S. H., Shao, M., Su, R., Wang, H. C.,
809 Wu, Y. S., Wahner, A., and Zhang, Y. H.: Explicit diagnosis of the local ozone production rate and the
810 ozone-NO_x-VOC sensitivities, *Sci. Bull.*, 63, 1067-1076, 10.1016/j.scib.2018.07.001, 2018.

811 Tan, Z. F., Lu, K. D., Hofzumahaus, A., Fuchs, H., Bohn, B., Holland, F., Liu, Y. H., Rohrer, F., Shao,
812 M., Sun, K., Wu, Y. S., Zeng, L. M., Zhang, Y. S., Zou, Q., Kiendler-Scharr, A., Wahner, A., and Zhang,
813 Y. H.: Experimental budgets of OH, HO₂, and RO₂ radicals and implications for ozone formation in
814 the Pearl River Delta in China 2014, *Atmos Chem Phys*, 19, 7129-7150, 10.5194/acp-19-7129-2019,
815 2019b.

816 Tan, Z. F., Fuchs, H., Lu, K. D., Hofzumahaus, A., Bohn, B., Broch, S., Dong, H. B., Gomm, S.,
817 Haseler, R., He, L. Y., Holland, F., Li, X., Liu, Y., Lu, S. H., Rohrer, F., Shao, M., Wang, B. L., Wang,
818 M., Wu, Y. S., Zeng, L. M., Zhang, Y. S., Wahner, A., and Zhang, Y. H.: Radical chemistry at a rural
819 site (Wangdu) in the North China Plain: observation and model calculations of OH, HO₂ and RO₂
820 radicals, *Atmos Chem Phys*, 17, 663-690, 10.5194/acp-17-663-2017, 2017.

821 Vaughan, S., Ingham, T., K. Whalley, L., Stone, D., Evans, M. J., Read, K. A., Lee, J. D., Moller, S. J.,
822 Carpenter, L. J., Lewis, A. C., Fleming, Z. L., and Heard, D. E.: Seasonal observations of OH and HO₂
823 in the remote tropical marine boundary layer, *Atmos. Chem. Phys.*, 12, 2149–2172, 10.5194/acp-12-
824 2149-2012, 2012.

825 Wang, F., Hu, R., Xie, P., Wang, Y., Chen, H., Zhang, G., and Liu, W.: Calibration source for OH
826 radical based on synchronous photolysis, *Acta Phys Sin-Ch Ed*, 69, 2020.

827 Wang, F. Y., Hu, R. Z., Chen, H., Xie, P. H., Wang, Y. H., Li, Z. Y., Jin, H. W., Liu, J. G., and Liu, W. Q.:
828 Development of a field system for measurement of tropospheric OH radical using laser-induced
829 fluorescence technique, *Opt. Express*, 27, A419-A435, 10.1364/oe.27.00a419, 2019.

830 Wang, J., Zhang, Y., Zhang, C., Wang, Y., Zhou, J., Whalley, L. K., Slater, E. J., Dyson, J. E., Xu, W.,
831 Cheng, P., Han, B., Wang, L., Yu, X., Wang, Y., Woodward-Massey, R., Lin, W., Zhao, W., Zeng, L.,
832 Ma, Z., Heard, D. E., and Ye, C.: Validating HONO as an Intermediate Tracer of the External Cycling
833 of Reactive Nitrogen in the Background Atmosphere, *Environ Sci Technol*, 10.1021/acs.est.2c06731,
834 2023.

835 Wang, T., Wei, X. L., Ding, A. J., Poon, C. N., Lam, K. S., Li, Y. S., Chan, L. Y., and Anson, M.:
836 Increasing surface ozone concentrations in the background atmosphere of Southern China, 1994-2007,
837 *Atmos Chem Phys*, 9, 6217-6227, 10.5194/acp-9-6217-2009, 2009.

838 Wang, Y., Hu, R., Xie, P., Chen, H., Wang, F., Liu, X., Liu, J., and Liu, W.: Measurement of
839 tropospheric HO₂ radical using fluorescence assay by gas expansion with low interferences, *J Environ
840 Sci (China)*, 99, 40-50, 10.1016/j.jes.2020.06.010, 2021.

841 Whalley, L. K., Furneaux, K. L., Goddard, A., Lee, J. D., Mahajan, A., Oetjen, H., Read, K. A., Kaaden,
842 N., Carpenter, L. J., Lewis, A. C., Plane, J. M. C., Saltzman, E. S., Wiedensohler, A., and Heard, D. E.:
843 The chemistry of OH and HO₂ radicals in the boundary layer over the tropical Atlantic Ocean, *Atmos
844 Chem Phys*, 10, 1555-1576, 2010.

845 Woodward-Massey, R., Sommariva, R., Whalley, L. K., Cryer, D. R., Ingham, T., Bloss, W. J., Ball, S.
846 M., Lee, J. D., Reed, C. P., Crilley, L. R., Kramer, L. J., Bandy, B. J., Forster, G. L., Reeves, C. E.,
847 Monks, P. S., and Heard, D. E.: Radical chemistry at a UK coastal receptor site – Part 1: observations
848 of OH, HO₂, RO₂, and OH reactivity and comparison to MCM model predictions, *Atmos. Chem. Phys.*,
849 10.5194/acp-2022-207, 2022a.

850 Woodward-Massey, R., Sommariva, R., Whalley, L. K., Cryer, D. R., Ingham, T., Bloss, W. J., Ball, S.
851 M., Lee, J. D., Reed, C. P., Crilley, L. R., Kramer, L. J., Bandy, B. J., Forster, G. L., Reeves, C. E.,
852 Monks, P. S., and Heard, D. E.: Radical chemistry at a UK coastal receptor site – Part 2: experimental
853 radical budgets and ozone production, *Atmos. Chem. Phys.*, 10.5194/acp-2022-213, 2022b.

854 Xia, M., Wang, T., Wang, Z., Chen, Y., Peng, X., Huo, Y., Wang, W., Yuan, Q., Jiang, Y., Guo, H., Lau,
855 C., Leung, K., Yu, A., and Lee, S.: Pollution-Derived Br₂ Boosts Oxidation Power of the Coastal
856 Atmosphere, *Environ Sci Technol*, 10.1021/acs.est.2c02434, 2022.

857 Xia, S.-Y., Zhu, B., Wang, S.-X., Huang, X.-F., and He, L.-Y.: Spatial distribution and source
858 apportionment of peroxyacetyl nitrate (PAN) in a coastal region in southern China, *Atmos Environ*, 260,
859 10.1016/j.atmosenv.2021.118553, 2021.

860 Xu, W., Ovadnevaite, J., Fossum, K. N., Lin, C., Huang, R.-J., Ceburnis, D., and O’Dowd, C.: Sea
861 spray as an obscured source for marine cloud nuclei, *Nature Geoscience*, 15, 282-286, 10.1038/s41561-
862 022-00917-2, 2022.

863 Yang, X., Lu, K., Ma, X., Gao, Y., Tan, Z., Wang, H., Chen, X., Li, X., Huang, X., He, L., Tang, M.,
864 Zhu, B., Chen, S., Dong, H., Zeng, L., and Zhang, Y.: Radical chemistry in the Pearl River Delta:
865 observations and modeling of OH and HO₂ radicals in Shenzhen in 2018, *Atmos Chem Phys*, 22,
866 12525-12542, 10.5194/acp-22-12525-2022, 2022a.

867 Yang, X., Lu, K., Ma, X., Gao, Y., Tan, Z., Wang, H., Chen, X., Li, X., Huang, X., He, L., Tang, M.,
868 Zhu, B., Chen, S., Dong, H., Zeng, L., and Zhang, Y.: Radical chemistry in the Pearl River Delta:
869 observations and 2 modeling of OH and HO₂ radicals in Shenzhen 2018, 10.5194/acp-2022-113, 2022b.

870 Yang, X., Lu, K., Ma, X., Liu, Y., Wang, H., Hu, R., Li, X., Lou, S., Chen, S., Dong, H., Wang, F.,
871 Wang, Y., Zhang, G., Li, S., Yang, S., Yang, Y., Kuang, C., Tan, Z., Chen, X., Qiu, P., Zeng, L., Xie, P.,
872 and Zhang, Y.: Observations and modeling of OH and HO₂ radicals in Chengdu, China in summer
873 2019, *The Science of the total environment*, 772, 144829-144829, 10.1016/j.scitotenv.2020.144829,
874 2021a.

875 Yang, Y., Li, X., Zu, K., Lian, C., Chen, S., Dong, H., Feng, M., Liu, H., Liu, J., Lu, K., Lu, S., Ma, X.,
876 Song, D., Wang, W., Yang, S., Yang, X., Yu, X., Zhu, Y., Zeng, L., Tan, Q., and Zhang, Y.: Elucidating
877 the effect of HONO on O₃ pollution by a case study in southwest China, *Sci Total Environ*, 756,
878 144127, 10.1016/j.scitotenv.2020.144127, 2021b.

879 Zeren, Y., Zhou, B., Zheng, Y., Jiang, F., Lyu, X., Xue, L., Wang, H., Liu, X., and Guo, H.: Does Ozone
880 Pollution Share the Same Formation Mechanisms in the Bay Areas of China?, *Environ Sci Technol*,
881 10.1021/acs.est.2c05126, 2022.

882 Zhang, G., Hu, R., Xie, P., Lou, S., Wang, F., Wang, Y., Qin, M., Li, X., Liu, X., Wang, Y., and Liu, W.:
883 Observation and simulation of HO_x radicals in an urban area in Shanghai, China, *Sci Total Environ*,
884 810, 152275, 10.1016/j.scitotenv.2021.152275, 2022a.

885 Zhang, G., Hu, R., Xie, P., Lu, K., Lou, S., Liu, X., Li, X., Wang, F., Wang, Y., Yang, X., Cai, H., Wang,
886 Y., and Liu, W.: Intercomparison of OH radical measurement in a complex atmosphere in Chengdu,
887 China, *Sci Total Environ*, 155924, 10.1016/j.scitotenv.2022.155924, 2022b.

888 Zhu, B., Huang, X.-F., Xia, S.-Y., Lin, L.-L., Cheng, Y., and He, L.-Y.: Biomass-burning emissions
889 could significantly enhance the atmospheric oxidizing capacity in continental air pollution, *Environ.*
890 *Pollut.*, 285, 10.1016/j.envpol.2021.117523, 2021.

891 Zhu, Y., Wang, Y., Zhou, X., Elshorbany, Y. F., Ye, C., Hayden, M., and Peters, A. J.: An investigation
892 into the chemistry of HONO in the marine boundary layer at Tudor Hill Marine Atmospheric
893 Observatory in Bermuda, *Atmos Chem Phys*, 22, 6327-6346, 10.5194/acp-22-6327-2022, 2022.

894 Zou, Z., Chen, Q., Xia, M., Yuan, Q., Chen, Y., Wang, Y., Xiong, E., Wang, Z., and Wang, T.: OH
895 measurements in the coastal atmosphere of South China: missing OH sinks in aged air masses,
896 EGU sphere, 2022, 1-47, 10.5194/egusphere-2022-854, 2022.
897